


Common reflection point mapping of the mantle transition zone using recorded and 3-D synthetic ScS reverberations

Journal Article

Author(s):

Haugland, Samuel M.; Ritsema, Jeroen; Sun, Daoyuan; Trampert, Jeannot; [Koroni, Maria](#) 

Publication date:

2020-01

Permanent link:

<https://doi.org/10.3929/ethz-b-000373113>

Rights / license:

[In Copyright - Non-Commercial Use Permitted](#)

Originally published in:

Geophysical Journal International 220(1), <https://doi.org/10.1093/gji/ggz467>

Common reflection point mapping of the mantle transition zone using recorded and 3-D synthetic ScS reverberations

Samuel M. Haugland,¹ Jeroen Ritsema,¹ Daoyuan Sun,² Jeannot Trampert³ and Maria Koroni⁴

¹Department of Earth and Environmental Sciences, University of Michigan, Ann Arbor, MI, 48103, USA. E-mail: samhaug@umich.edu

²Laboratory of Seismology and Physics of Earth's Interior, School of Earth and Space Sciences, University of Science and Technology China, Hefei, 230026 Anhui, China

³Department of Earth Sciences, University of Utrecht, 3512 JE Utrecht, The Netherlands

⁴Department of Earth Sciences, ETH Zürich, 8092 Zürich, Switzerland

Accepted 2019 October 14. Received 2019 September 10; in original form 2019 February 4

SUMMARY

The method of ScS reverberation migration is based on a ‘common reflection point’ analysis of multiple ScS reflections in the mantle transition zone (MTZ). We examine whether ray-theoretical traveltimes, slownesses and reflection points are sufficiently accurate for estimating the thickness H of the MTZ, defined by the distance between the 410- and 660-km phase transitions. First, we analyse ScS reverberations generated by 35 earthquakes and recorded at hundreds of seismic stations from the combined Arrays in China, Hi-NET in Japan and the Global Seismic Network. This analysis suggests that H varies by about 30 km and therefore that dynamic processes have modified the large-scale structure of the MTZ in eastern Asia and the western Pacific region. Second, we apply the same procedure to spectral-element synthetics for PREM and two 3-D models. One 3-D model incorporates degree-20 topography on the 410 and 660 discontinuities, otherwise preserving the PREM velocity model. The other model incorporates the degree-20 velocity heterogeneity of S20RTS and leaves the 410 and 660 flat. To optimize reflection point coverage, our synthetics were computed assuming a homogeneous grid of stations using 16 events, four of which are fictional. The resolved image using PREM synthetics resembles the PREM structure and indicates that the migration approach is correct. However, ScS reverberations are not as strongly sensitive to H as predicted ray-theoretically because the migration of synthetics for a model with degree-20 topography on the 410 and 660: H varies by less than 5 km in the resolved image but 10 km in the original model. In addition, the relatively strong influence of whole-mantle shear-velocity heterogeneity is evident from the migration of synthetics for the S20RTS velocity model and the broad sensitivity kernels of ScS reverberations at a period of 15 s. A ray-theoretical approach to modelling long-period ScS traveltimes appears inaccurate, at least for continental-scale regions with relatively sparse earthquake coverage. Additional modelling and comparisons with SS precursor and receiver function results should rely on 3-D waveform simulations for a variety of structures and ultimately the implementation of full wave theory.

Key words: ScS reverberations; Phase transition topography; Mantle transition zone; Migration; 3-D synthetics.

1 INTRODUCTION

The phase transitions from olivine to wadsleyite at about 410 km depth (the ‘410’ from hereon) and from ringwoodite to bridgmanite and ferropericlasite at 660 km depth (the ‘660’ from hereon) produce the strongest seismic discontinuities in the mantle transition zone (MTZ). Changes in temperature and composition modify the depths of the 410 and 660. Therefore, maps of the undulations of these

phase transitions constrain heat and mass transfer across the MTZ. In particular, the thickness of the MTZ, defined as the distance between the 410 and 660 and labelled H in this paper, has been estimated routinely by seismologists. See Deuss (2009) and Kind & Li (2015) for recent reviews.

Shear-wave reflections at the 410 and 660 arriving before the surface reflection SS (the so-called SS precursors, e.g. Flanagan & Shearer 1998; Chambers *et al.* 2005; Schmerr & Garnero 2007;

Day & Deuss 2013) or between multiple ScS reflections off the core and surface (i.e. ScS, ScS₂ and ScS₃, the so-called ScS reverberations; e.g. Revenaugh & Jordan 1989; Revenaugh & Sipkin 1994a; Katzman *et al.* 1998; Courtier & Revenaugh 2006, 2007; Bagley *et al.* 2013) are frequently used for studying the layered structure of the upper mantle. These phases provide sampling in between events and seismic stations which is helpful for imaging the mantle beneath oceans inaccessible to receiver function studies.

Theoretical and forward modelling studies have demonstrated that ray theory may not be sufficiently accurate for the modelling of SS precursors. SS phases have relatively long periods ($T > 15$ – 20 s) and broad Fresnel zones (e.g. Neele *et al.* 1997; Zhao & Chevrot 2003) so they are sensitive to seismic velocity variations and discontinuity structure well beyond rays and ray reflection points. Experiments with waveform synthetics computed for 3-D seismic models indicate that ray theory underestimates traveltime delays by up to factor of two (Bai *et al.* 2012) and that SS precursors may interfere with core phases (Koroni *et al.* 2017). Koroni & Trampert (2016) showed that the contributions of the 3-D velocity structure and the boundary topography to the traveltimes are not necessarily additive since the X-shaped boundary kernels of SS precursors depend on the background model.

It is likely that ray-theoretical modelling of ScS reverberations is also inexact. Like SS precursors, ScS reverberations have long propagation paths through the lower mantle, they are recorded as relatively long-period signals, and their sensitivity kernels are similarly complex. Fig. 1 illustrates this for ScS₂ and the corresponding bottom-side reflection at the 660, ScS₆₆₀ScS. The ScS reverberations are sensitive to velocity structure outside the geometric ray paths, especially near the core. The sensitivity is relatively low at the surface reflection point of ScSScS.

In this study, we explore how well H can be determined using ScS reverberations. We determine the variation of H in eastern Asia and the western Pacific region using waveforms recorded by hundreds of seismometers in the region and a common-reflection-point migration technique that relies on ray-theoretical calculations of reflection points and traveltimes of long-period ScS reverberations. We validate the map of H by analysing synthetic seismograms with the same method and assumptions. The synthetics are computed for two seismic models, which include either topography on the 410 and 660 or shear-velocity variations in the mantle.

2 WAVEFORM SETS

Deep-focus (>100 km) earthquakes with vertical dip-slip fault mechanisms produce the clearest ScS reverberations in low-pass filtered ($T > 15$ s) transverse-component seismograms. The relatively short durations of deep earthquakes and the separation of the depth phases (e.g. sScS, sScS₂) from the direct phases (e.g. ScS, ScS₂) simplify the analysis. Fig. 2 shows a representative recording we have examined in this study. The ScS reverberations arrive between 500 and 3600 s after the earthquake origin time. Their amplitudes decrease with increasing arrival time due to geometric spreading and attenuation. No other major body-wave phases have the same traveltimes but trailing Love waves can interfere with sScS and ScS₂ especially for shallow and intermediate-depth (<200 km) earthquakes.

The low-amplitude arrivals between the main phases are reflections from discontinuities in the MTZ. We define five windows with energy from these reflections. Signals arriving within 250 s before ScS₂ and ScS₃ and within 250 s after sScS, sScS₂ and sScS₃ are

bottom-side and top-side reflections, respectively. Only ScS₂ and its bottom-side reflections in window 2 reflect once and exactly mid-way between source and receiver and can be uniquely identified in a waveform. Bottom-side and top-side reflections for the other phases may have similar traveltimes depending on earthquake depths and the depths of the reflectors.

To minimize migration artefacts near the 410 and 660 and to estimate H as accurately as possible, we do not use earthquakes between 180 and 220 km. We opt to use earthquakes between 100 and 180 km to optimize data coverage. This compromises the quality of the image of the MTZ between about 450 and 550 km depth but it does not affect our estimate of H (Fig. S1).

2.1 Recorded ScS reverberations

Our data set includes 21 307 waveforms produced by 35 events since 2009 with magnitudes between 6 and 8 and focal depths between 105 and 664 km (Table 1). These events occurred in the subduction zones of Sumatra, Java and the western Pacific (Fig. 3a) and were recorded by the China National Seismic Network, regional seismic arrays in China, the broad-band Hi-net array in Japan and GSN stations in the region.

Fig. 3(b) highlights the model region where the number of ScS reverberation reflection points in circular caps with radii of 3° is higher than 500. Sampling is densest, hence resolution is expected to be highest beneath eastern China and the Pacific Ocean between the Philippines and Japan. The circular regions with anomalously high (>2000) reflection counts coincide with earthquakes. Here, most reflection are source-side reflections for single earthquakes so resolution is probably low despite high reflection density.

2.2 Computed ScS reverberations

To minimize computational cost, we consider only 12 of the 35 earthquakes indicated with asterisks in Table 1. The seismic source parameters of the events are taken unmodified from the CMT catalogue (Ekström & Nettles 2015). We add four fictitious events (Events 36–39) in the eastern part of the model region (Fig. 3c) to optimize the event distribution. These four fictitious events are at 600 km depth and have the same source mechanism as Event 18.

Since we calculate the synthetic seismograms for a uniform grid of stations, the ScS reflection point coverage by the synthetics is nearly uniform throughout the model region (Fig. 3d). We expect therefore that the migrations of the synthetics are not strongly affected by limited sampling and that they expose primarily imaging artefacts due to the intrinsic resolution of ScS reverberations and the simplifications made in the modelling of the waveforms.

3 METHODS

3.1 Data processing

We obtain transverse-component velocity records by rotating the N/S and E/W component records. We filter these records using a second-order Butterworth filter with a low-pass corner frequency of 0.067 Hz (i.e. signals have periods longer than 15 s). Since the ScS reverberations have relatively low amplitudes, we use the method of Schultz & Gu (2013) to improve their signal-to-noise ratios and to suppress interfering Love waves and other signals with slownesses different than the slownesses of ScS reverberations (see Fig. S2).

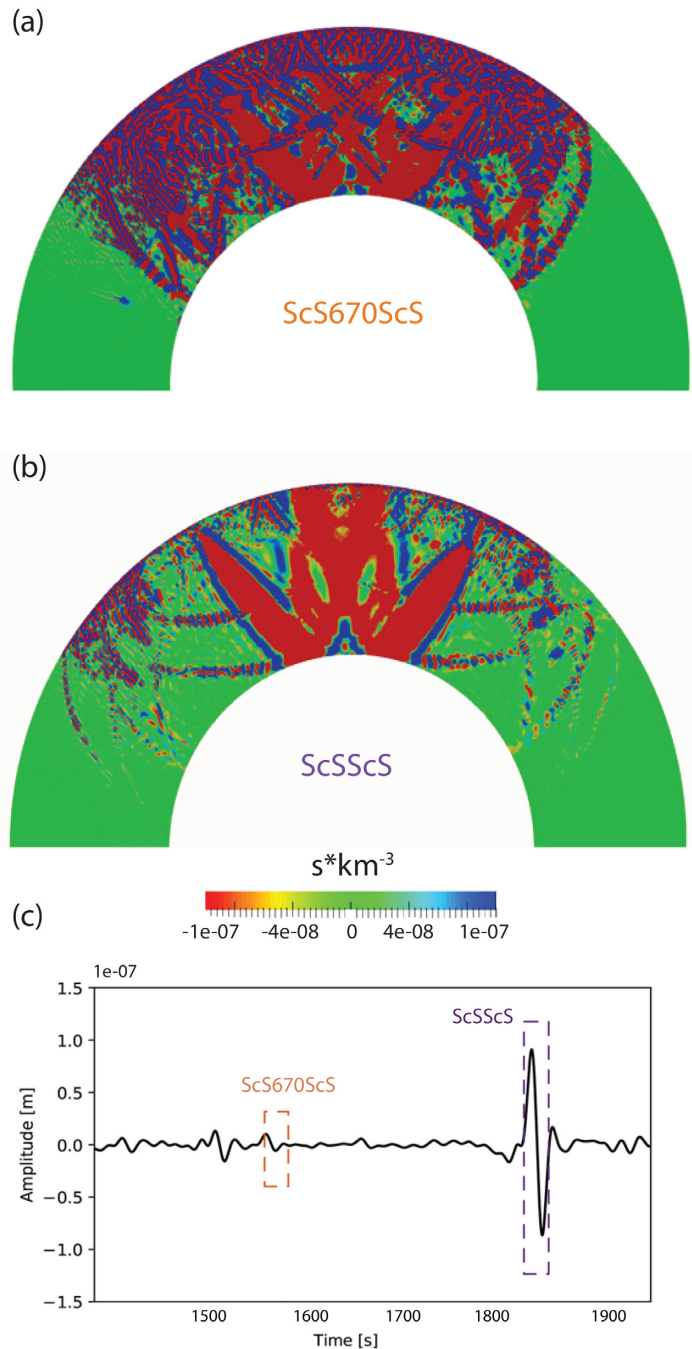


Figure 1. Traveltime sensitivity kernels computed with the adjoint method for (a) ScS₆₆₀ScS and (b) ScSScS calculated using the PREM synthetic shown in (c) for an earthquake at 620 km depth, an epicentral distance of 49°, and a period of 15 s. The squares indicate the 40-second wide segments around ScS₆₆₀ScS and ScSScS used in the kernel calculations of (a) and (b).

We deconvolve signals in each of the five intervals by the corresponding main phases to remove the effects of earthquake finiteness on the waveforms. The deconvolution involves a spectral division with a water level 10 per cent of the highest spectral amplitude (see Fig. S3 for a comparison of unprocessed and deconvolved reverberation windows). It allows us to combine earthquakes with different source durations but the deconvolution may produce spurious sidelobes above and below the 410 and 660 reflections. After these steps, we exclude traces with signal-to-noise ratios lower than 3 from the analysis and examine all seismograms individually for quality.

3.2 Common-reflection-point migration

Our approach is similar to that of Wang *et al.* (2017) who studied the MTZ beneath the Japan Sea. We apply it to a larger area to obtain a regional perspective of the variation of H , albeit it at lower spatial resolution.

We determine the migration image by stacking 500-s wide wave segments with signals of reverberations in windows 1 through 5 whose ray-theoretical reflection points are in the same circular bins with radii of 3°. The weight of a trace in a stack is inversely proportional to the number of possible reflections at the same depth (i.e. 1

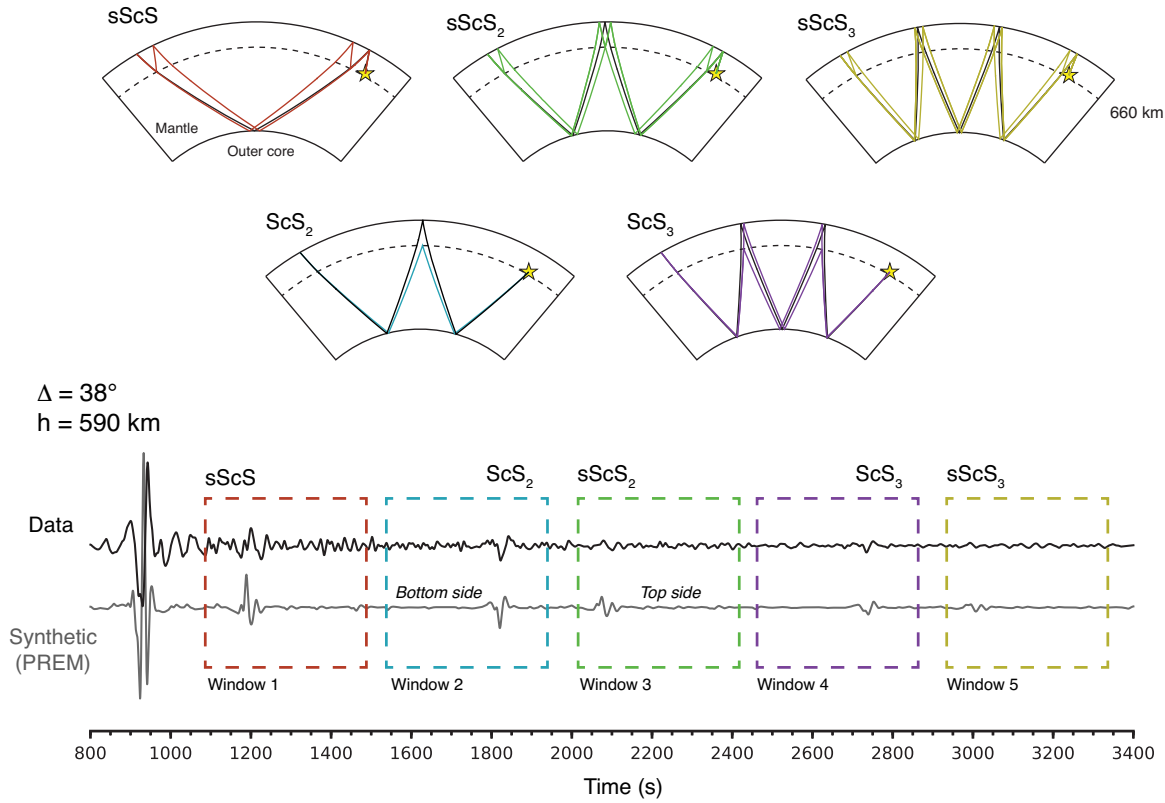


Figure 2. Top panel: ray diagrams of the five main ScS multiples and corresponding reverberations for an epicentral distance of 60° . Bottom panel: transverse-component recording and PREM synthetic of the 2012-08-04 Okhotsk earthquake (depth = 590 km; $M_W = 7.7$) at China National Seismic Network station GYA (Guiyang, Yunnan Province) at a distance of 38° . In this recording, the ScS reverberations considered in this study arrive between 1100 s and 3400 s. The dashed squares indicate the reverberation windows 1, 2, 3, 4 and 5. The labels ‘Bottom side’ and ‘Top side’ indicate bottom-side reflections arriving before ScS₂ in window 2 and top-side reflections following sScS₂ in window 3, respectively. Similar reflections are present in the other windows.

for ScS₂; 1/2 for sScS and ScS₃; 1/3 for sScS₂ and 1/4 for sScS₃). The bins overlap as their centers form a grid with a uniform spacing of 1.5° in the model region. We calculate the reflection points and align the ScS reverberations relative to the main phases using the TauP utilities (Crotwell *et al.* 1999) for the PREM velocity structure.

We measure H from the centroids of the stacked signals corresponding to the 410 and 660. We find waveform correlation measurements not to be more precise and that measuring H from the peaks in the stacks is not robust. By trial and error, we determine that our estimates of H have uncertainties of at least 10 km. The uncertainties depend on the widths and variable shapes of the stacked signals and the presence of side lobes. The quality of the stack is determined by the number of waveforms, and their variability in windows 1 through 5 due to the effects of wave attenuation and complex propagation.

4 MIGRATION OF RECORDED SCS REVERBERATIONS

4.1 Vertical cross-sections

Fig. 4 shows the stacked waveforms for cross sections A–A’ through the interior of the model region where sampling is best and the quality of the migration image is highest. The image reveals boundaries of variable strengths near 275, 400, 500 and 650 km depth. The negative polarity signals just above and below these boundaries are most likely side-lobes due to signal deconvolution.

The horizons at 275 and 500 km depth are slightly weaker than the boundaries at 400 and 650 km depth and they are double peaked. It is possible that the boundary near 500 km depth is associated with the wadsleyite to ringwoodite phase transition and that its partition into two signals has the same origin as the splitting of the 520-km discontinuity observed by Deuss & Woodhouse (2001) in SS precursors. However, as discussed in the supplementary material, by including data for earthquakes shallower than 180 km depth, the boundary near 500 km may be an artefact due to traveltimes degeneracy of source- and receiver-side reflections. For the same reasons, we suspect the boundary near 275 km depth to be a result of erroneous projection of reflections from the 410 to shallower depths.

The 410 and 660 should be resolved unaffected for the range of source depths we have selected. Their amplitudes vary laterally, which has also been observed in migrations of SS precursors (Dokht *et al.* 2016, 2018), S-to-P conversions (Zhang *et al.* 2017) and ScS₂/ScS amplitude ratios (Chaves *et al.* 2016). However, the 410 and 660 are present throughout the image allowing us to estimate H over a wide area of the model region.

4.2 Estimates of H

Fig. 5 shows histograms and a map of H with interpolated values resolved in the circular bins. The mean of H is 253 km, consistent with the mean of 250 km estimated from global receiver functions (e.g. Tauzin *et al.* 2012) given uncertainties. H deviates from the

Table 1. Events used in data analysis. Asterisks indicate events included in simulations.

	Lat (°N)	Lon (°E)	Time (UTC)	Depth (km)	M_W	Region
1	−7.23	123.04	2017-10-24 10:47:47	549	6.7	Banda Sea
2	27.78	139.80	2017-09-07 17:26:49	451	6.1	Bonin Islands
3	9.38	123.95	2017-05-20 01:06:14	533	6.0	Philippines
4	4.46	122.57	2017-01-10 06:13:47	612	7.3	Celebes Sea
5	−7.31	123.38	2016-12-05 01:13:04	526	6.3	Banda Sea
6*	−4.86	108.16	2016-10-19 00:26:01	614	6.6	Java Sea
7	24.94	142.01	2016-08-04 16:24:33	510	6.3	Volcano
8	−21.97	178.20	2016-05-28 05:38:50	405	6.9	Fiji Islands
9*	23.09	94.87	2016-04-13 13:55:17	136	6.9	Myanmar
10	36.52	70.36	2015-10-26 09:09:42	231	7.5	Hindu Kush
11	27.83	140.49	2015-05-30 11:23:02	664	7.8	Bonin Islands
12	25.54	122.45	2014-12-10 21:03:39	256	6.1	Taiwan
13	28.39	138.87	2014-06-30 19:55:33	527	6.2	Bonin Islands
14	27.42	127.32	2014-03-02 20:11:22	118	6.5	Ryukyu Islands
15	4.64	123.40	2013-11-03 11:03:40	556	6.0	Celebes Sea
16	12.27	141.71	2013-10-06 16:38:10	118	6.0	Mariana
17*	53.14	152.90	2013-10-01 03:38:21	578	6.7	Okhotsk
18*	52.14	151.57	2013-05-24 14:56:31	632	6.7	Okhotsk
19*	18.77	145.29	2013-05-14 00:32:26	611	6.8	Mariana Islands
20	42.73	131.06	2013-04-05 13:00:02	571	6.3	Russia/China
21*	42.78	143.15	2013-02-02 14:17:34	105	6.9	Hokkaido
22*	49.75	145.31	2012-08-14 02:59:38	590	7.7	Okhotsk
23*	−7.56	146.80	2011-12-14 05:04:17	128	7.1	Eastern New Guinea
24	−6.36	126.75	2011-08-30 06:57:41	467	6.9	Banda Sea
25*	26.98	139.87	2011-01-12 21:32:54	524	6.5	Bonin Islands
26*	6.56	123.36	2010-07-29 07:31:56	615	6.6	Mindanao
27	6.711	123.48	2010-07-23 22:08:11	610	7.3	Philippines
28	19.35	144.75	2010-03-08 09:47:10	446	6.1	Mariana Islands
29*	42.59	130.70	2010-02-18 01:13:19	578	6.9	Northeast China
30	−17.24	178.45	2009-11-09 10:44:54	591	7.3	Fiji
31	−6.11	130.42	2009-10-24 14:40:44	140	6.9	Banda Sea
32	4.08	122.53	2009-10-07 21:41:14	586	6.8	Celebes Sea
33	6.67	123.50	2009-10-04 10:58:00	635	6.6	Mindanao
34*	−7.20	123.46	2009-08-28 01:51:19	640	6.9	Banda Sea
35	33.14	138.05	2009-08-09 10:55:56	302	7.1	Honshu
36*	10.00	90.00	Mechanism of #18	600	6.7	Bay of Bengal
37*	35.00	110.00	Mechanism of #18	600	6.7	Central China
38*	35.00	80.00	Mechanism of #18	600	6.7	Tibet
39*	50.00	100.00	Mechanism of #18	600	6.7	Northern Mongolia

mean by as much as 15 km but H is between 242 and 260 km for 90 per cent of the bins.

The circular anomalies near earthquakes coincide with regions where the number of reflections is higher than 5000 (see Fig. S1a). Since these anomalies are determined primarily by source-side reflections from single earthquakes, not by averaging multiple reverberation types and waveforms from multiple events, H is poorly resolved in these regions despite high reflection counts.

5 MIGRATION OF COMPUTED SCS REVERBERATIONS FOR 3-D MODELS

5.1 Spectral-element method synthetics

To evaluate the fidelity of the migration results illustrated in Figs 4 and 5, we apply the migration approach described in Section 3 to seismograms computed with the spectral element method (Komatitsch & Tromp 2002). In the analysis, we process and migrate the synthetics in the same manner as the recordings and reproduce maps of H from the centroids of the 410 and 660 signals in the stacked synthetic waveforms. Since the synthetic waveforms have

less variability, the migrations are cleaner and we can measure H with an uncertainty of about 5 km, much lower than for the data.

We compute the synthetics using a modified version of SPECfEM3D-Globe, which allows us to introduce shear-velocity heterogeneity and arbitrary topography at all first-order discontinuities of the reference model (Koroni & Trampert 2016). The mesh and processing parameters (NEX=400 and NPROC=10) are set so that the synthetics are accurate down to a period of about 10 s and include the effects of attenuation, ellipticity, gravity, rotation, ocean loading and surface topography.

We explore three seismic models for the mantle. The first model is PREM in which wave speed varies with depth only and the 410 and 660 are at depths of 400 and 670 km, respectively. PREM has an additional discontinuity at 220 km depth but no discontinuities within the MTZ. The second model, called PREM-D, has the PREM velocity structure but we add topography on the 410 and the 660. The topography is a random spherical harmonic degree 20 model with an amplitude of ± 15 km. We use the same topography model for the 410 and 660 discontinuities but with opposite sign. Hence, the thickness H has peak-to-peak variations of up to 30 km (Fig. 6). In the third model, called PREM-V, the 410 and 660 are horizontal and at 400 and 670 km depth as in PREM but the velocity structure

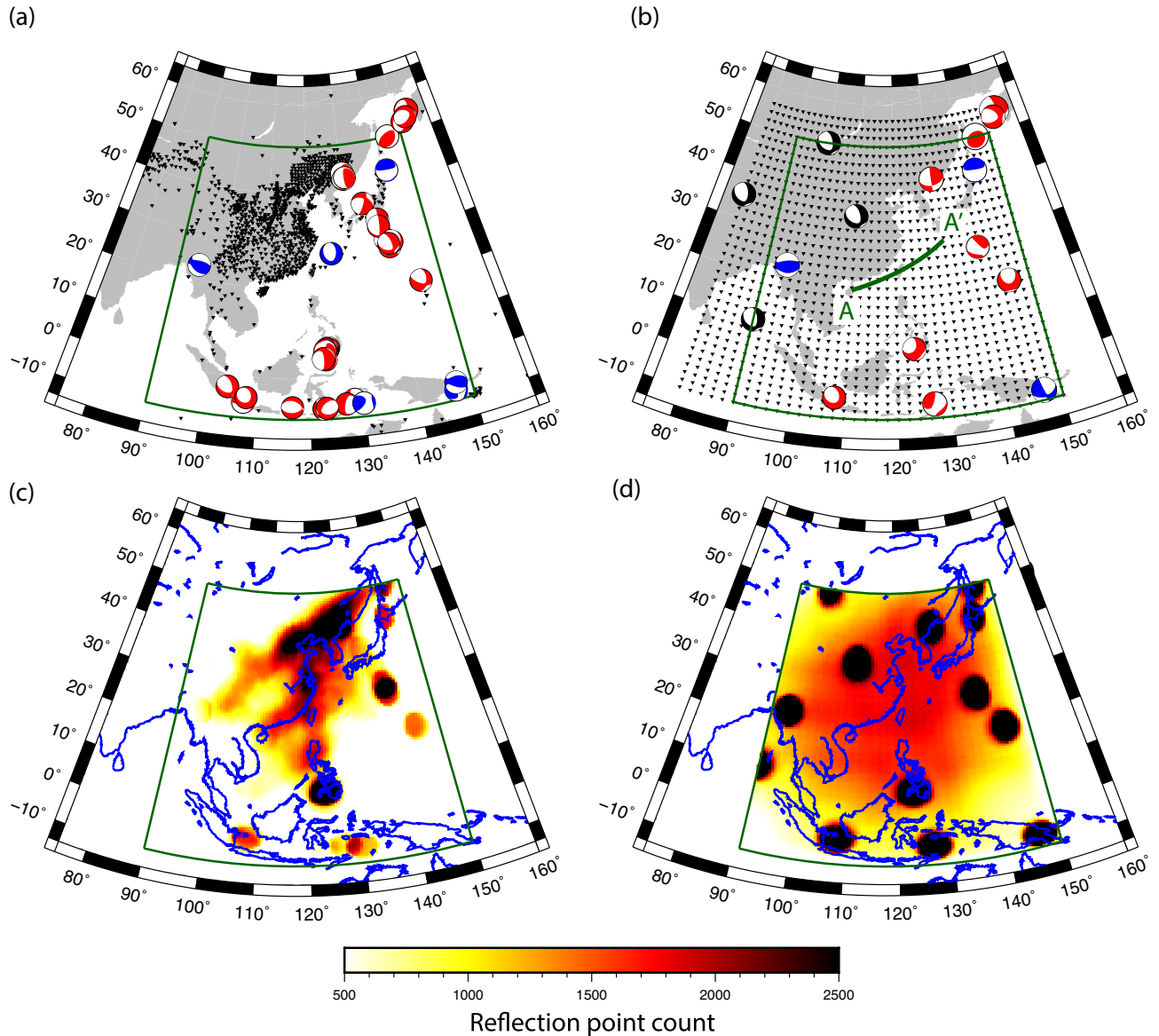


Figure 3. Maps of the study region with earthquake locations and mechanisms (shown as ‘beach ball diagrams’) and locations of stations (triangles) in (a) the Arrays of China, Hi-net, and GSN used to analyse recorded waveforms and (b) a rectangular grid used to explore imaging artefacts. Beach ball diagrams for earthquakes shallower and deeper than 300 km are colored blue and red, respectively. The black earthquakes in panel (b) are four fictitious events at 600 km depth. The dark green box indicates the region for which we show migration results. The green line indicates the orientation of transect A–A’ used to display vertical cross section of migration images (see Figs S1 and S4). Panels (c) and (d) show ScS reflection point counts for the data and synthetics, respectively.

is the degree-20 velocity structure of tomographic model S20RTS (Ritsema *et al.* 1999) plus CRUST2.0 (Bassin *et al.* 2000) (Fig. 7). Fig. S4 compares reverberation windows for synthetics computed with the PREM, PREM-D and PREM-V models.

5.2 Migration of synthetics

Fig. 8 shows the migration results for the PREM model. As in Fig. 4, we show the map and histograms of the MTZ thickness. Reflectors near 210, 410 and 660 are the only high-amplitude structures as expected. The side lobes surrounding the 410 and 660 originate from signal deconvolution that is also applied to the PREM synthetics. The thickness H of the MTZ has a median value of 270 km, which is identical to PREM. The resolved perturbations from the

mean are less than 2 km and smaller than the measurement uncertainty. Since we reproduce an upper-mantle discontinuity structure similar to PREM and artificial perturbations of H within measurement uncertainties, we conclude that the migration procedure is, in principle, robust.

The migration of waveforms computed for model PREM-D (Fig. 9) renders a transition zone with a median thickness of 271 km. Like the PREM simulations, this is also close to the PREM value of 270 km. The resolved variation of the MTZ thickness of about 5 km slightly exceeds the 5-km uncertainty in measuring the depth of the 410 and 660 from the stacks. It grossly underestimates the 30-km prescribed variation in PREM-D (compare Figs 6c to 9c). Moreover, the resolved variation of H does not resemble the pattern of H in PREM-D (compare Figs 6a and 9a). For example, the MTZ is thin beneath Korea and northeastern China (at 40N, 125E) and beneath

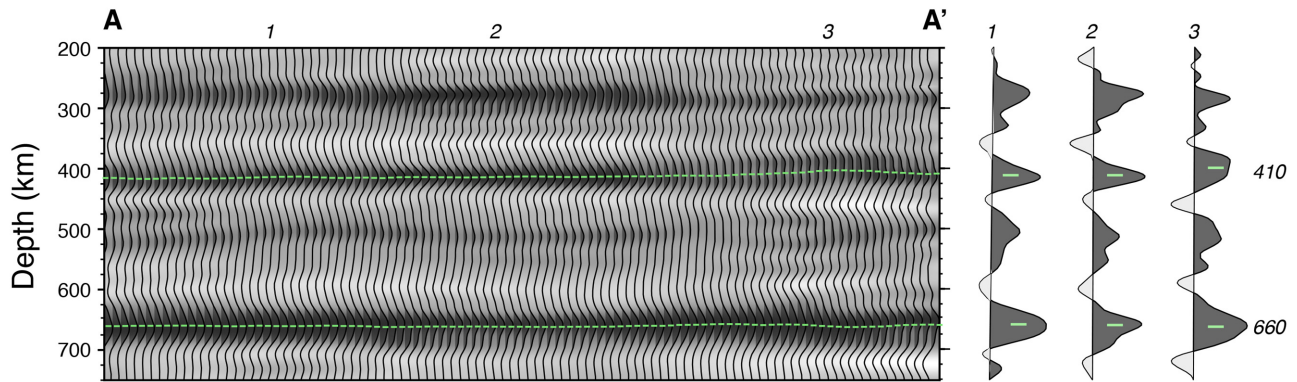


Figure 4. Cross section through the common reflection point image along the transect A–A' spanning 23° drawn in Fig. 3(b). A grey scale is used to fill the waveforms. Positive and negative polarity peaks are shaded black and white, respectively. The green triangles indicate the peak amplitudes of the 410 and the 660. We do not show the image for depths shallower than 200 km and deeper than 800 km because artefacts from the migration are strong. On the right, we show enlarged stacks of reverberations at positions 1, 2 and 3 along transect A–A'.

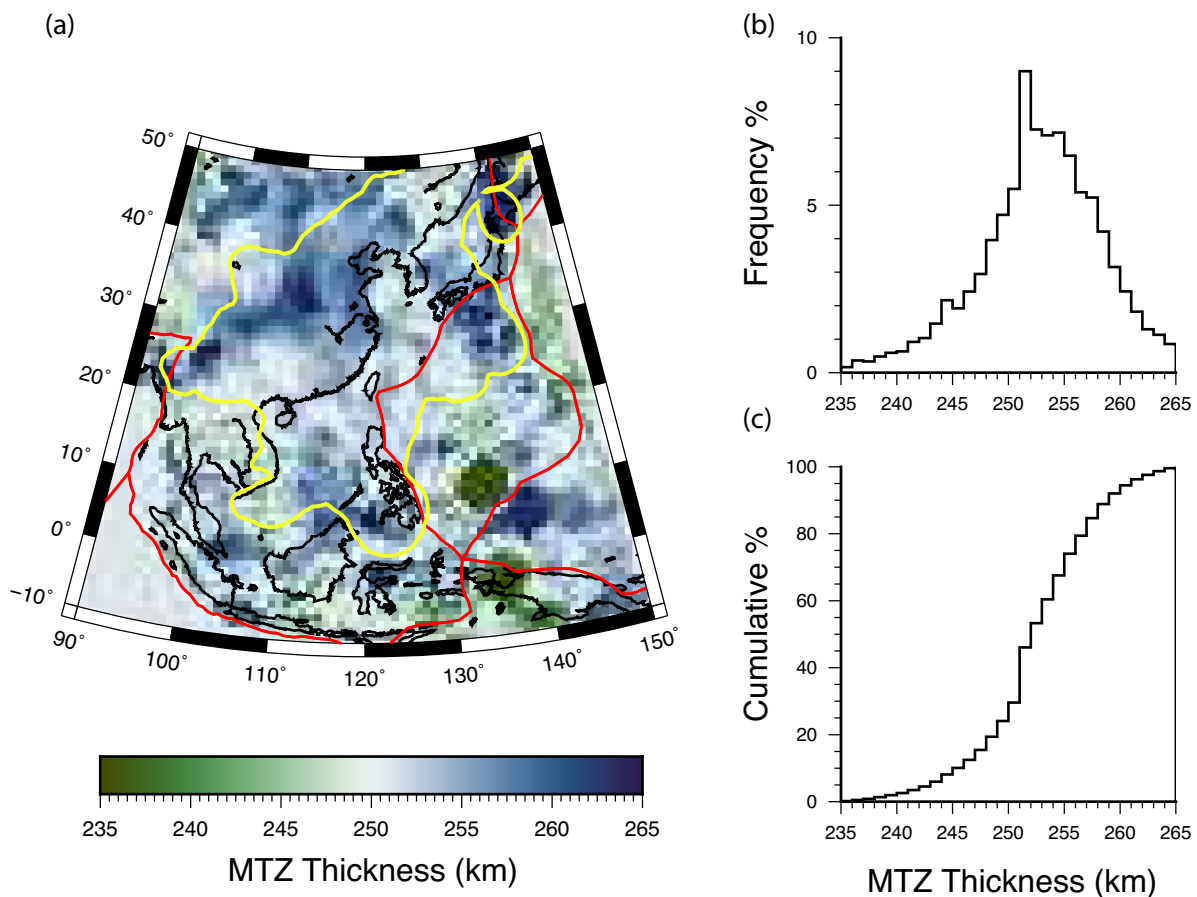


Figure 5. (a) Map of the resolved thickness H of the MTZ for data from events in Table 1. The common reflection point image along transect A–A' is shown in Fig. 4. The yellow contour surrounds the region in which the number of reflection points is at least 500. (b and c) Frequency and cumulative histograms of the resolved MTZ thickness values.

central China (at 35°N , 95°E) in PREM-D but H has high values in these regions in the migrated image. In the image the lowest values of H in the MTZ are between Japan and the Philippines whereas the MTZ has an average thickness in this region in PREM-D. This indicates that the ScS multiples are insensitive to the degree-20 variations of the MTZ thickness.

The image obtained from migrating PREM-V synthetics (Fig. 10) features a median thickness of the MTZ of about 265 km. This is

5 km smaller than the PREM value because on average the shear velocity is relatively high in the MTZ beneath the study region for model PREM-V. The degree-20 velocity structure of S20RTS projects as stronger variation in the MTZ thickness than the degree-20 thickness variations of PREM-D. The MTZ thickness varies by about 7 km, whereas it is 5 km for the PREM-D model. There is no obvious correlation between the resolved MTZ thickness and the S20RTS shear velocity structure in the MTZ (i.e., Fig. 10a versus

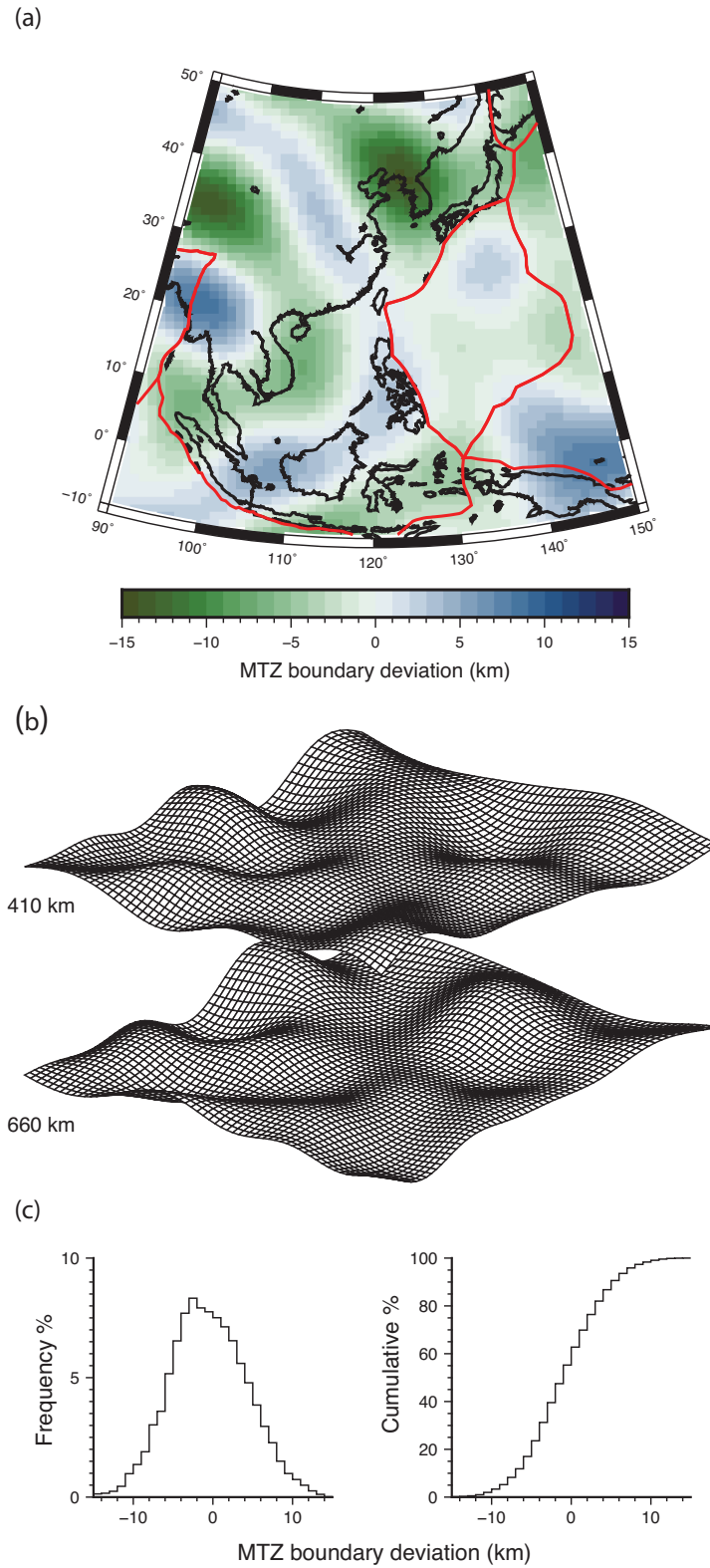


Figure 6. (a) Map and (b) surface rendering view of the opposite topography on the 410 and 660 boundaries prescribed in model PREM-D. (c) Frequency and cumulative histograms of the prescribed thickness of the MTZ shown in (a) and (b).

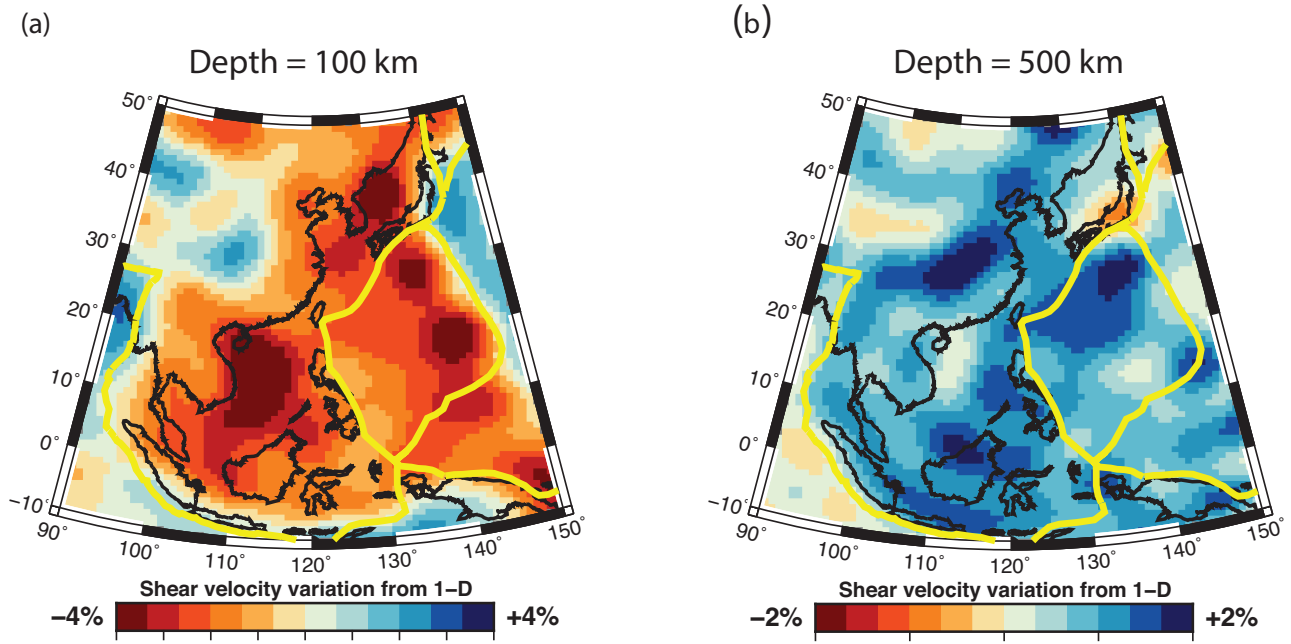


Figure 7. Map-view of the shear-velocity structure of model PREM-V at (a) 100 km depth and (b) 500 km depth.

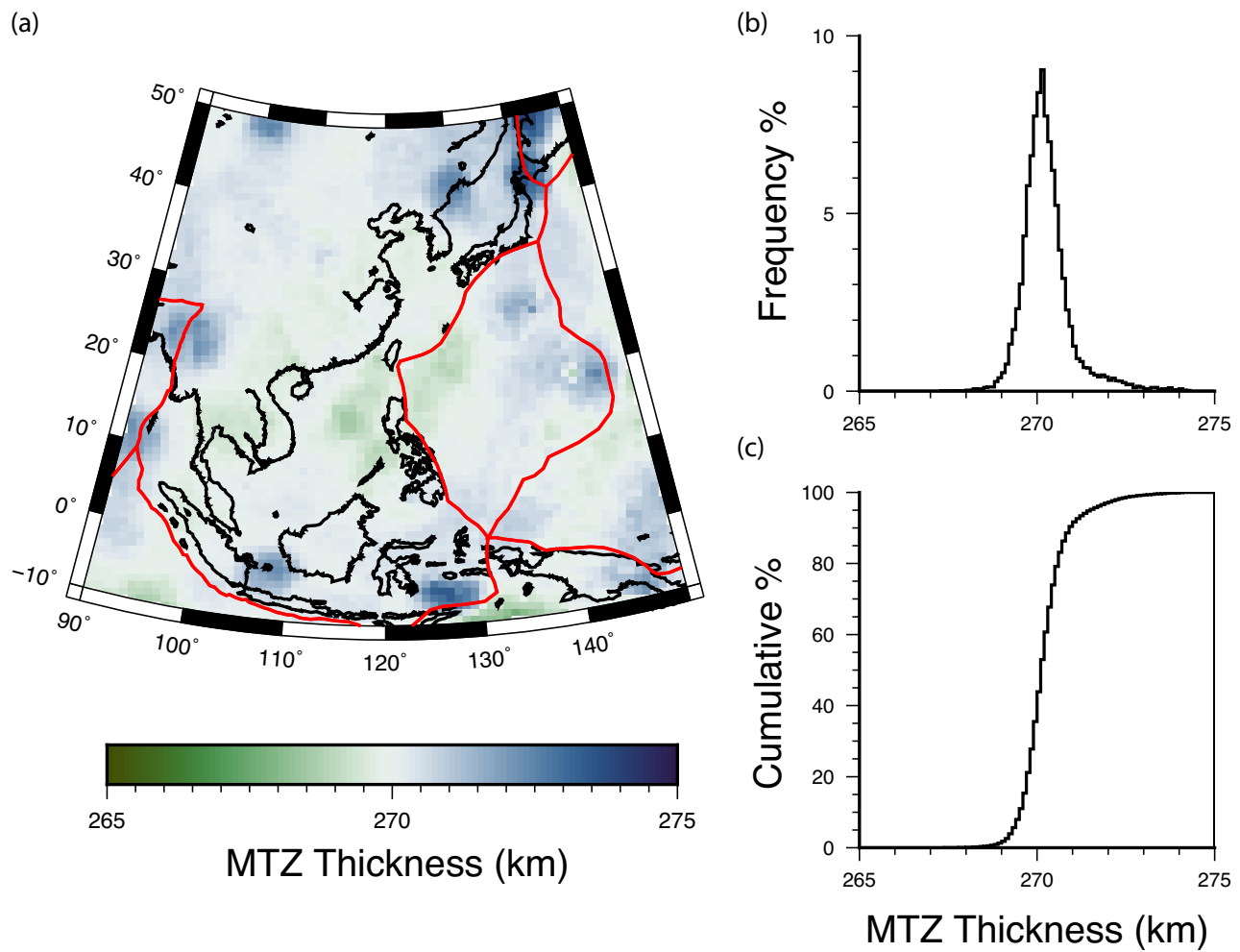


Figure 8. (a) Resolved MTZ thickness H obtained by migrating PREM synthetics for earthquakes in Table 1 denoted by asterisks. Panels (b) and (c) show percent and cumulative percent histograms of H .

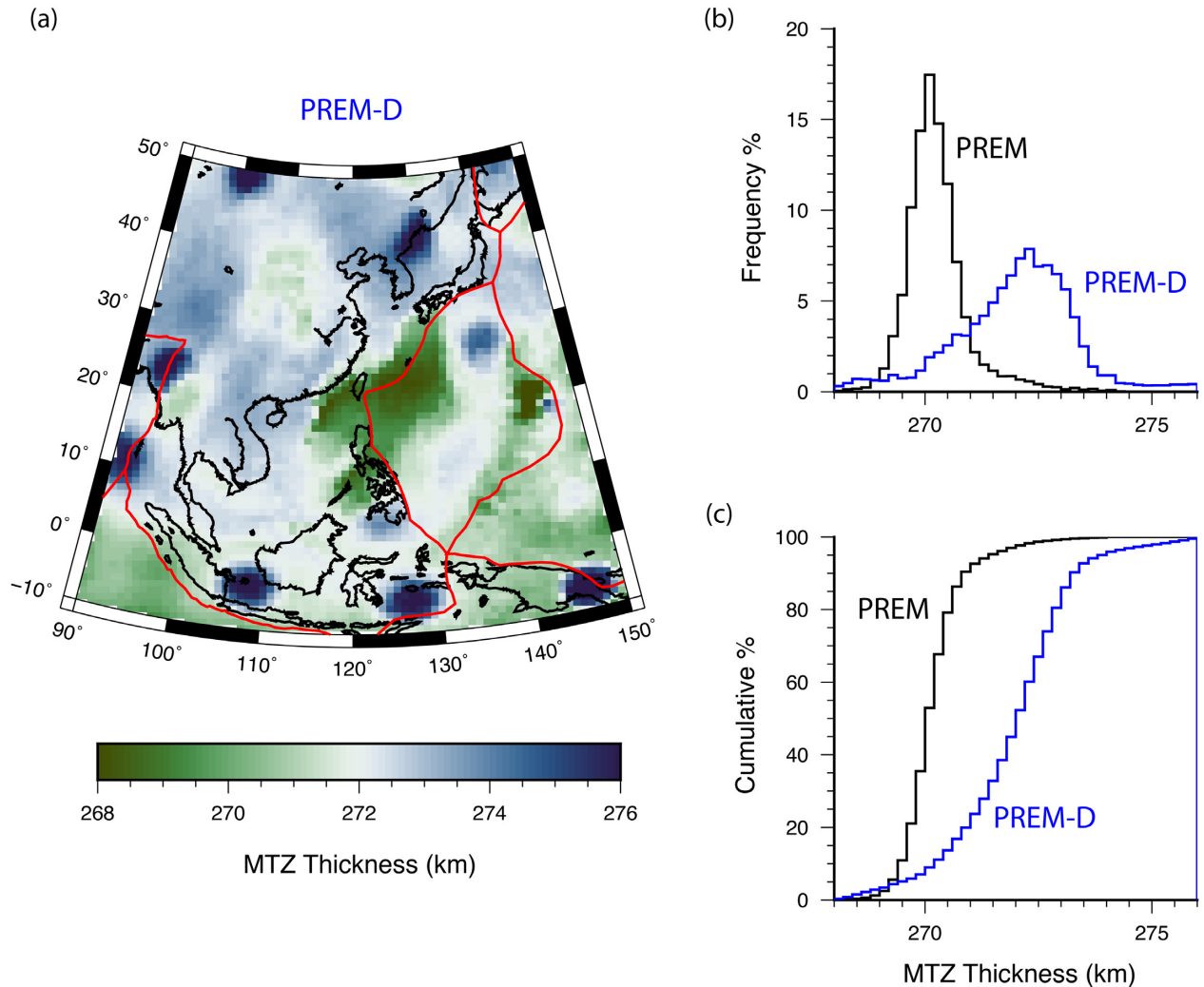


Figure 9. (a) Resolved MTZ thickness H obtained by migrating the waveforms for model PREM-D with prescribed topography on the 410 and 660 (see Fig. 6). (b) Frequency and (c) cumulative histograms of the estimated H for models PREM (in black) (see Fig. 8) and PREM-D (in blue) shown in (a).

Fig. 7b) so it appears that the traveltime variations due to velocity heterogeneity in the mantle are mapped as variations in H in an unpredictable manner.

6 DISCUSSION AND CONCLUSIONS

ScS reverberations are useful seismic phases to study the layered structure of the upper mantle. In regions with high seismicity, they place constraints that are complementary to analyses of SS precursors and receiver functions. However, as with the analysis of SS precursors, ray-theoretical approximations in the modelling can render significant modelling artefacts. Multiple ScS phases propagate along long paths through the mantle, they are recorded at relatively long periods, and their Fresnel zones are therefore wide.

In this paper, we have compared estimates of the thickness H between the 410 and 660 phase transitions based on similarly processed recorded and synthetic seismograms using a common reflection point migration technique. We have focused the analyses on eastern Asia and the western Pacific region. In this region with active plate collision, H is expected to vary strongly. The imaging of H is facilitated by available waveform data produced by numerous

deep earthquakes and recorded by hundreds of stations in various networks.

Our analysis of 21 307 waveforms for 35 earthquakes suggests that the mantle transition zone beneath the study region has an average thickness of 250 km. H has long-wavelength variations of about 18 km, which corresponds to temperature variations of roughly 150 K following Bina & Helffrich (1994). The MTZ appears to be thickest beneath northeastern China, Indonesia, the Philippine Sea and the Pacific Ocean east of the Philippines, where relatively cool oceanic lithosphere has descended into the MTZ. The widening of the MTZ beneath northeastern China has also been inferred from receiver function studies by Li & Yuan (2003), Ai *et al.* (2003) and Shen *et al.* (2008), and the SS precursor studies by Gu *et al.* (2012) and Dokht *et al.* (2016). The thick MTZ beneath Indonesia is consistent with the receiver function study by Saita *et al.* (2002) and a previous study of ScS reverberations by Ohtaki *et al.* (2002) but a quantitative comparison between modelling result is difficult due to differences in used data types and sampling of the mantle.

Our processing of synthetic waveforms for 3-D models of the mantle indicates that the resolved structure of H is highly uncertain. Velocity structure in the mantle and phase-transition topography contribute to the delay times of multiple ScS waves in a complex

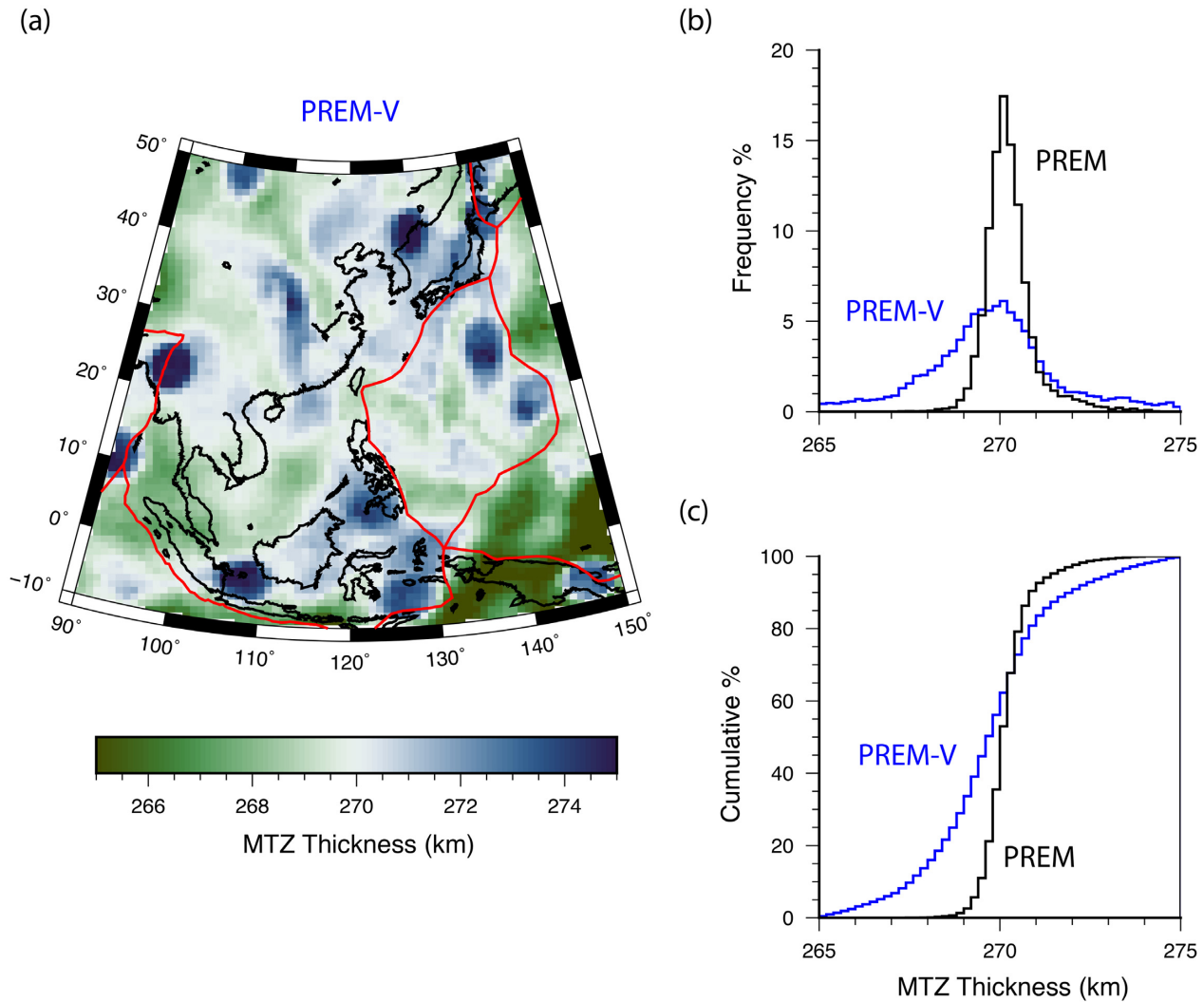


Figure 10. (a) Resolved MTZ thickness H obtained by migrating the waveforms for model PREM-V. (b) Frequency and (c) cumulative histograms of the estimated MTZ thickness for models PREM (in black) (see Fig. 8) and PREM-V (in blue) shown in (a).

manner that is not predictable by ray theory. The resolved image derived from synthetics for tomographic model S2ORTS, a model with smooth velocity variations but horizontal phase boundaries, features peak-to-peak variation in H of about 6 km. This is about a third of the variation seen in the waveform data image and demonstrates that shear-velocity heterogeneity in the mantle is projected as relatively strong topography on the 410 and 660.

The migration of synthetics for a model with degree-20 variation of H indicate that that ScS reverberations are not strongly sensitive to long-wavelength perturbations of the MTZ thickness. Whereas thickness of the MTZ varies by as much as 30 km in the input model, the variation in the resolved image is six times smaller at about 5 km, comparable to the intrinsic uncertainty of the migration method. Therefore, shear-velocity heterogeneity in the mantle may overwhelm the contribution of 410 and 660 undulations to traveltime delays of ScS reverberations.

Synthetic tests for two models do not permit a full characterization of the modelling artefacts. Our modification of the SPECFEM3D-Globe software limits us to calculating synthetic seismograms for velocity heterogeneity and topography on the 410 and 660 at spatial scales longer than spherical harmonic degree 20. We expect that the modelling artefacts are large as well for

finer-scale undulations in the 410 and 660 produced by 100-km scale slabs of subducted lithosphere or velocity variations which are evident in regional seismic tomography (e.g. Zhao 2012; Chen *et al.* 2015). An accurate migration of ScS reverberations (and other long-period body-wave phases) require joint analyses of 410 and 660 topography and shear-velocity structure which account for the broad sensitivities of multiple ScS waves to velocity structure and on high-resolution shear-velocity models of the mantle (e.g. Chen *et al.* 2015).

ACKNOWLEDGEMENTS

The data from China National Seismic Network used in this study are provided by Data Management Centre of China National Seismic Network at Institute of Geophysics, China Earthquake Administration (doi:10.11998/SeisDmc/SN, <http://www.seisdmc.ac.cn>) (Zheng *et al.* 2010) and the waveform data are processed at the Supercomputing Center of USTC. The Hi-net network is operated by the National Research Institute for Earth Science and Disaster Resilience (<http://www.hinet.bosai.go.jp>). The GSN data are available at the IRIS Data Management Center (www.iris.edu). This research has been supported by NSF grant EAR-1644829 to JR.

SH acknowledges travel support from a Turner Student Grant and a Rackham Travel Grant at UM. DS is supported by National Natural Science Foundation of China 41874050. MK is supported by grant received from the European Research Council (ERC) under the European Union's Horizon 2020 research and innovation programme (grant agreement No 714069). Our imaging results will be made available after this manuscript has been accepted for publication. We thank Editor Sidao Ni and two anonymous reviewers for helpful comments.

REFERENCES

- Ai, Y., Zheng, T., Xu, W., He, Y. & Dong, D., 2003. A complex 660 km discontinuity beneath northeast China, *Earth planet. Sci. Lett.*, **212**, 63–71.
- Bagley, B., Courtier, A.M. & Revenaugh, J., 2013. Seismic shear wave reflectivity structure of the mantle beneath northeast China and the northwest Pacific, *J. geophys. Res.*, **118**, 5417–5427.
- Bai, L., Zhang, Y. & Ritsema, J., 2012. An analysis of SS precursors using spectral-element method seismograms, *Geophys. J. Int.*, **188**(1), 293–300.
- Bassin, C., Laske, G. & Masters, G., 2000. The current limits of resolution for surface wave tomography in North America, *EOS, Trans. Am. Geophys. Un.*, **81**, F897.
- Bina, C.R. & Helffrich, G., 1994. Phase transition Clapeyron slopes and transition zone seismic discontinuity topography, *J. geophys. Res.*, **99**(B8), 15 853–15 860.
- Chambers, K., Deuss, A. & Woodhouse, J.H., 2005. Reflectivity of the 410-km discontinuity from PP and SS precursors, *J. geophys. Res.*, **110**(B2).
- Chaves, C.A. & Ritsema, J., 2016. The influence of shear velocity heterogeneity on ScS2/ScS amplitude ratios and estimates of Q in the mantle, *Geophys. Res. Lett.*, **43**(15), 7997–8005.
- Chen, M., Niu, F., Liu, Q., Tromp, J. & Zheng, X., 2015. Multiparameter adjoint tomography of the crust and upper mantle beneath East Asia: 1. Model construction and comparisons, *J. geophys. Res.*, **120**(3), 1762–1786.
- Courtier, A.M. & Revenaugh, J., 2006. A water-rich transition zone beneath the eastern United States and Gulf of Mexico from multiple ScS reverberations, in *Earths Deep Water Cycle, Geophys. Monogr. Series*, vol. 168, pp. 181–193, eds Jacobsen, S.D. & van der Lee, S., AGU.
- Courtier, A.M. & Revenaugh, J., 2007. Deep upper-mantle melting beneath the Tasman and Coral Seas detected with multiple ScS reverberations, *Earth planet. Sci. Lett.*, **259**, 66–76.
- Crotwell, H. P., Owens, T. J. & Ritsema, J., 1999. The TauP Toolkit: Flexible seismic travel-time and ray-path utilities, *Seismol. Res. Lett.*, **70**, 154–160.
- Day, E.A. & Deuss, A., 2013. Reconciling PP and PP precursor observations of a complex 660 km seismic discontinuity, *Geophys. J. Int.*, **194**(2), 834–838.
- Deuss, A., 2009. Global observations of mantle discontinuities using SS and PP precursors, *Surv. Geophys.*, **30**, 301–326.
- Deuss, A. & Woodhouse, J., 2001. Seismic observations of splitting of the mid-transition zone discontinuity in Earth's mantle, *Science*, **294**, 354–357.
- Dokht, R.M.H., Gu, Y.J. & Sacchi, M.D., 2016. Waveform inversion of SS precursors: an investigation of the northwestern Pacific subduction zones and intraplate volcanoes in China, *Gondwana Res.*, **40**, 77–90.
- Dokht, R.M.H., Gu, Y.J. & Sacchi, M.D., 2018. Migration imaging of the Java subduction zones, *J. geophys. Res.*, 1540–1558.
- Ekström, G. & Nettles, M., 2015. Long-period moment-tensor inversion: the Global CMT Project, in *Encyclopedia of Earthquake Engineering*, pp. 1360–1371, Springer.
- Flanagan, M.P. & Shearer, P.M., 1998. Global mapping of topography on transition zone velocity discontinuities by stacking SS precursors, *J. geophys. Res.*, **103**(B2), 2673–2692.
- Gu, Y.J., Okeler, A. & Schultz, R., 2012. Tracking slabs beneath northwestern Pacific subduction zones, *Earth planet. Sci. Lett.*, **331**, 269–280.
- Katzman, R., Zhao, L. & Jordan, T.H., 1998. High-resolution, two-dimensional vertical tomography of the central Pacific mantle using ScS reverberations and frequency-dependent travel times, *J. geophys. Res.*, **103**, 17 933–17 971.
- Kind, R. & Li, X., 2015. Deep Earth structure-transition zone and mantle discontinuities, in *Treatise on Geophysics*, Vol. 1, pp. 591–618, ed. Schubert, G., Elsevier B.V.
- Komatitsch, D. & Tromp, J., 2002. Spectral-element simulations of global seismic wave propagation—I. Validation, *Geophys. J. Int.*, **149**, 390–412.
- Koroni, M. & Trampert, J., 2016. The effect of topography of upper-mantle discontinuities on SS precursors, *Geophys. J. Int.*, **204**(1), 667–681.
- Koroni, M., Bozdağ, E., Paulssen, H. & Trampert, J., 2017. Sensitivity analysis of seismic waveforms to upper-mantle discontinuities using the adjoint method, *Geophys. J. Int.*, **210**(3), 1965–1980.
- Li, X. & Yuan, X., 2003. Receiver functions in northeast China – implications for slab penetration into the lower mantle in the northwest Pacific subduction zone, *Earth planet. Sci. Lett.*, **216**(4), 679–691.
- Neele, F., de Regt, H. & Van Decar, J., 1997. Gross errors in upper-mantle discontinuity topography from underside reflection data, *Geophys. J. Int.*, **129**(1), 194–204.
- Ohtaki, T., Suetsugu, D., Kanjo, K. & Purwana, I., 2002. Evidence for a thick mantle transition zone beneath the Philippine Sea from multiple ScS waves recorded by JISNET, *Geophys. Res. Lett.*, **29**(13), 24–1–24–4.
- Revenaugh, J. & Jordan, T.H., 1989. A study of mantle layering beneath the western Pacific, *J. geophys. Res.*, **94**, 5787–5813.
- Revenaugh, J. & Sipkin, S.A., 1994. Seismic evidence for silicate melt atop the 410-km mantle discontinuity, *Nature*, **369**, 474–476.
- Ritsema, J., van Heijst, H.J. & Woodhouse, J.H., 1999. Complex shear wave velocity structure imaged beneath Africa and Iceland, *Science*, **286**(5446), 1925–1928.
- Saita, T., Suetsugu, D., Ohtaki, T., Takenaka, H., Kanjo, K. & Purwana, I., 2002. Transition zone thickness beneath Indonesia as inferred using the receiver function method for data from the JISNET regional broadband seismic network, *Geophys. Res. Lett.*, **29**(7), 19–1–19–4.
- Schmerr, N. & Garnero, E.J., 2007. Upper mantle discontinuity topography from thermal and chemical heterogeneity, *Science*, **318**(5850), 623–626.
- Schultz, R. & Gu, J., 2013. Flexible, inversion-based Matlab implementation of the Radon transform, *Comput. Geosci.*, **52**, 437–442.
- Shen, X., Zhou, H. & Kawakatsu, H., 2008. Mapping the upper mantle discontinuities beneath China with teleseismic receiver functions, *Earth, Planets, Space*, **60**(7), 713–719.
- Tauzin, B., Debayle, E. & Wittlinger, G., 2008. The mantle transition zone as seen by global Pds phases: No clear evidence for a thin transition zone beneath hotspots, *J. geophys. Res.*, **113**, B08309, doi:10.1029/2007JB005364.
- Wang, X., Li, J. & Chen, Q.F., 2017. Topography of the 410 km and 660 km discontinuities beneath the Japan Sea and adjacent regions by analysis of multiple-ScS waves, *J. geophys. Res.*, **122**, 1264–1283.
- Zhang, H., Ni, S., Chu, R. & Schmandt, B., 2017. An algorithm for computing synthetic body waves due to underside conversion on an undulating interface and application to the 410 km discontinuity, *Geophys. J. Int.*, **210**(3), 1858–1871.
- Zhao, D., 2012. Tomography and dynamics of Western-Pacific subduction zones, *Monogr. Environ. Earth Planets*, **1**, 1–70.
- Zhao, L. & Chevrot, S., 2003. SS-wave sensitivity to upper mantle structure: implications for the mapping of transition zone discontinuity topographies, *Geophys. Res. Lett.*, **30**(11), doi:10.1029/2003GL017223.
- Zheng, X.F., Yao, Z.X., Liang, J.H. & Zheng, J., 2010. The role played and opportunities provided by IGP DMC of China National Seismic Network in Wenchuan earthquake disaster relief and researches, *Bull. seism. Soc. Am.*, **100**(5B), 2866–2872.

SUPPORTING INFORMATION

Supplementary data are available at [GJI](https://doi.org/10.1002/gji.122011724) online.

Figure S1. Illustration of the traveltime degeneracy between (a) the topside reflection at the 660, ScSS₆₆₀S and (b) the topside reflection at a discontinuity at depth x , sS _{x} SScS for an earthquake at depth

h . (c) indicates values for h and x when the traveltimes of sS_xSScS and $ScSS_{660}S$ (blue) or $ScSS_{410}S$ (orange) are the same. Panels (d) and (e) are cross sections of migrated PREM synthetics along transect A–A', as discussed in Section 4.1. Panels (d) and (e) are determined for waveforms from earthquakes with depths between 100 and 300 km and earthquakes deeper than 300 km, respectively. The orange ellipse in (d) indicates a migration artefact in the MTZ.

Figure S2. Transverse component record sections of Event 6 (a) before and (b) after radon transformation. Major expected ScS phases are indicated by red lines.

Figure S3. Synthetic reverberation windows for a station 20° away from a 578 km deep earthquake. Each reverberation window is shown with the unprocessed trace in black and the deconvolved

trace in red. Reverberation windows are: (a) ScS_2 , (b) ScS_3 , (c) $sScS$, (d) $sScS_2$ and (e) $sScS_3$. ScS Reverberations from the 410 and 660 are labelled in (a) and (c).

Figure S4. Synthetic ScS_2 reverberation window for a station 20° away from a 578 km deep earthquake shown for PREM (black), PREM-D (red) and PREM-V (blue). All windows are normalized on ScS_2 .

Please note: Oxford University Press is not responsible for the content or functionality of any supporting materials supplied by the authors. Any queries (other than missing material) should be directed to the corresponding author for the paper.